



Manufacture of zircon bulk parts and scaffolds by digital light processing

E. Rosado^{a,b,*}, R. Moreno^b, T. Graule^a, M. Stuer^a

^a Swiss Federal Laboratories for Materials Science and Engineering, Empa, Dübendorf, Switzerland

^b Instituto de Cerámica y Vidrio (ICV), Consejo Superior de Investigaciones Científicas (CSIC), Kelsen 5, 28049, Madrid, Spain

ARTICLE INFO

Handling Editor: Dr P Colombo

Keywords:

Zircon
Digital light processing
Slurries
Rheology
Debinding

ABSTRACT

Zircon (ZrSiO_4) is a low cost and widely available ceramic raw material used in thermal applications due to its low thermal conductivity and high thermal shock resistance. The aim of the present work was to obtain solid and reticular zircon pieces by digital light processing (DLP), scarcely reported in the literature. For this aim, the dispersion of zircon powders in two different solvents (benzyl alcohol and cyclohexanol) was studied using different UV-curable polymeric systems. The effect of different dispersant concentrations as well as different dispersion/homogenisation methods were evaluated by rheological characterisation. Bulk bodies and scaffolds were obtained by DLP, studying the effect of different printing parameters on the quality and resolution of the produced parts. Debinding and sintering steps were optimised using different thermal cycles. Dense zircon scaffolds (>96%TD) were obtained from the cyclohexanol based slurries. Finally, the obtained materials were characterised in terms of crystallographic composition and microstructure.

1. Introduction

Zircon (ZrSiO_4) is a widely available ceramic raw material in mineral sand form, low cost (1–3 €/kg) [1], whose properties such as its low thermal conductivity (5.1 W/m.K at room temperature and 3.5 W/m.K at 1000 °C) [2], high dissociation temperature (1675 °C) [3], low coefficient of thermal expansion ($4.99 \times 10^{-6} \text{ K}^{-1}$) [4] or its resistance to thermal shock and chemical attack [2,5] make it an ideal material for high temperature applications. Thus, zirconium silicate is widely used as a refractory material in the steel and glass industry [3,5–7]. Recent studies have even demonstrated its qualities for obtaining thermal barrier coatings by plasma spraying techniques that could be used in the aeronautical or automotive sectors [8,9].

Given its application as a refractory or thermal barrier material, in addition to its thermal properties, zircon must also exhibit good mechanical performance so that it resists impact shock (e.g. from glass molten particles inside furnaces) or certain stresses to which this material is subjected through industrial processes. For this, high densities must be achieved in the final parts or coatings, which is complicated in the case of zirconium silicate due to its low sinterability. Therefore, high green densities must be previously achieved favouring its subsequent densification by sintering, for which the processing of the starting powder as well as its shaping become key steps. In this sense, in the last

decades, numerous works have been reported in which zircon-based materials were formed by means of different shaping techniques.

One of the main strategies to favour the zircon sintering is the addition of secondary minority phases, such as silica [10], alumina [11], titania [12] or zirconia [13], which form a transient liquid phase at high temperatures in order to promote the densification of the zircon. On the other hand, different processing techniques have been used, such as high-energy ball milling for the activation of the starting powders [14] and their subsequent axial [11,12] or isostatic pressing [10,12,15,16]. Different colloidal processing routes have also been employed to enable a more exhaustive control of particle packing in order to increase the green density of the obtained materials. In this way, pure zircon powders have been reported to be obtained by colloidal sol-gel synthesis routes from organic and inorganic precursors [17], by reverse micelle processes [18], micro-emulsion processes [19] or liquid aerosol hydrolysis [20], generally resulting in nanomaterials with enhanced mechanical properties. In addition, different colloidal shaping techniques have been reported using suspensions such as slip casting [21–23], gelcasting [24] or suspension plasma spraying [8,9], in which a thorough rheological study of the slurries allows minimising the structural defects and obtaining high green densities to favour the sintering process [25]. Furthermore, it is worth mentioning that for all these zircon materials obtained by different techniques and pressureless sintering without

* Corresponding author. Instituto de Cerámica y Vidrio (ICV), Consejo Superior de Investigaciones Científicas (CSIC), Kelsen 5, 28049, Madrid, Spain.

E-mail addresses: eduardo.rosado@icv.csic.es (E. Rosado), rmoreno@icv.csic.es (R. Moreno), Thomas.Graule@empa.ch (T. Graule), Michael.Stuer@empa.ch (M. Stuer).

<https://doi.org/10.1016/j.oceram.2023.100536>

Received 28 November 2023; Accepted 24 December 2023

Available online 31 December 2023

2666-5395/© 2023 The Authors. Published by Elsevier Ltd on behalf of European Ceramic Society. This is an open access article under the CC BY-NC-ND license (<http://creativecommons.org/licenses/by-nc-nd/4.0/>).

additives, no density values higher than 96 % were reported. Higher density values have only been reported for those densified by non-conventional sintering techniques such as SPS [14,26] or hot pressing of powders [27,28], with the consequent higher production costs.

Due to the different applications for which zircon is intended, some of them requiring the forming of complex shapes or to adapt to the dimensions and morphologies of other in-contact components, the study of its shaping by additive manufacturing techniques is also gaining importance nowadays. Still, very few works regarding AM of zircon parts have been reported in the literature. To the best of our knowledge, only Basar Ozkan et al. reported obtaining SiO_2 - ZrSiO_4 parts by vat-photopolymerization [29] and Italo Leite de Camargo et al. reported obtaining zircon-mullite parts by stereolithography-based 3D printing [30], none of them obtaining pure crystalline dense zircon parts.

Regarding the different AM techniques for parts production, those based on stereolithography such as digital light processing (DLP) could be the most suitable for zircon 3D printing, in which photocurable suspensions are used to build the desired morphologies layer by layer. Furthermore, DLP is considered to be the AM technique with the highest printing resolution, enabling tiny complex morphologies to be obtained with a very precise surface finish [31,32]. In this way, careful rheological control of the mixture homogeneity and colloidal dispersion of the starting powder in the UV-resins would make it possible to obtain defect-free materials with high green densities so that the zircon could be densified using conventional sintering techniques. For this, the photosensitive suspensions should meet certain requirements, such as containing at least 40 vol% solids in order to favour the debinding process without generating microdefects or delamination [33–37] and having viscosities below 3 Pa s so that they flow adequately in the printing vat to ensure the homogeneity and adhesion of the successive micrometric layers [35,36,38]. Another key stage is the post-processing of the obtained pieces with the design of thermal cycles with different steps and appropriate heating rates so that the organic compounds are progressively volatilised, allowing the ceramic particles to approach without cracking or shape deformations [33,34,39,40].

Thus, the aim of the present work is to obtain pure zircon bulk parts and scaffolds by DLP for the first time, as well as their full densification by conventional sintering. Different photopolymerizable systems were studied by using different non-reactive solvents (pore formers) in the formulations that could favour the debinding step, as well as a rheological study of the produced slurries to optimise the printing process. Thermal debinding was also studied according to the suspension composition and the densification grade and microstructure of the final parts were evaluated.

2. Experimental

2.1. Materials and reagents

The starting ceramic raw material was a commercial zircon powder (Zircobit® MO/S, Industrie Bitossi S. p.A., Italy) composed of 64.3 ± 0.5 ZrO_2 , 32.5 ± 0.5 SiO_2 , 2.0 ± 0.5 Al_2O_3 , 0.15 ± 0.03 TiO_2 , 0.07 ± 0.01 Fe_2O_3 (oxide wt%). Its mean particle size (d_{v50}) is 1.1 ± 0.2 μm with an average density of 4.46 g/cm^3 and a specific surface area of 6.9 m^2/g . The surface area was measured by one-point BET method (Monosorb Surface Area Analyser MS-13, Quantachrome, USA), the density by He-pycnometry (Multipycnometer, Quantachrome, USA), and the particle size distribution was measured by laser diffraction (Mastersizer 3000 analyser, Malvern, UK). Particle size measurements were performed using benzyl alcohol as dispersion medium and studying the effect of dispersant concentration and different homogenisation methods.

The polyacrylic resin was prepared in the laboratory by mixing the following components with respective relative concentrations: 25–35 wt % of either benzyl alcohol (BA) or cyclohexanol (CH) (Sigma-Aldrich, Switzerland) as low volatile and non-reactive organic solvents, 45–55 wt

% 3-methyl-1,5-pentanediol diacrylate (MPDDA, Genomer 1226, Rahn AG, Switzerland) as a low viscosity monomer, 20 wt% polyetherpolyol acrylate (Genomer*5695, Rahn AG, Switzerland) used as an oligomer to increase the reactivity of the resin, and 3 wt% diphenyl 2,4,5-trimethylbenzoyl phosphine (Genocure*TPO-L, Rahn AG, Switzerland) as a photoinitiator to promote free radical formation. Solsperse 41,000 (Lubrizol Advanced Materials S. L., Spain) was used as a dispersing agent.

2.2. UV-curable slurry preparation and optimisation

The liquid phase was firstly prepared by mixing the solvent (BA or CH), the monomer and the oligomer with a magnetic stirrer, to obtain organic mixtures. Four different mixtures were prepared (BA25, CH25, BA35, CH35) to vary the solvent type and its concentration in wt%. The optimal amount of dispersant was also added and homogenised into the organic solution (1 wt% with respect to zircon powder, determined from the dispersion study described in the following section). Then, the zircon powder was added to the liquid phase by using a propeller mixer (RW 20 digital, IKA-Werke, Germany). Once the fresh-prepared slurries were obtained, a planetary mill (PM 400, Retsch, Germany) was used at 300 rpm for 20 min to break down the agglomerates and fully disperse the ceramic powder in the organic mixture. After planetary mill treatment, the photoinitiator was added and the slurries were left homogenizing on a rolling bench for 24 h with 3 mm zirconia balls as milling medium (1/3 in volume with respect to the suspension).

2.3. Slurries characterisation

The particle size distribution of the commercial zircon powder was studied in benzyl alcohol medium (6 vol% ZrSiO_4) by laser diffraction (Mastersizer 3000 analyser, Malvern, UK), with and without the addition of different amounts of dispersant and after the different mechanical processes that were used to optimise the slurries (40 vol% ZrSiO_4). The diluted slurries were homogenised only by keeping them for 72 h in rolling bench with 3 mm zirconia balls.

The rheological behaviour of the different slurries (without photoinitiator) was studied using a rotational rheometer (MCR302, Anton Paar, Austria) with a concentric cylinder measuring system (CC27/T200/SS). Measurements were performed under controlled shear rate (CR) at 25 °C using the following program: from 1 to 500 s^{-1} in 150 s, maintaining at 500 s^{-1} for 60 s, and finally from 500 to 1 s^{-1} in 150 s.

2.4. Digital light processing (DLP)

The different ceramic pieces (bars and scaffolds) were printed by DLP using the custom-made equipment Cerafab 7500 (Lithoz GmbH, Austria), with a lateral resolution of 20 μm and UV-light source of $\lambda = 365$ nm. The printing parameters were varied for each ceramic/polymeric system using energy doses from 12 to 30 mJ/cm^2 , exposure times from 1 to 4 s and intensities from 2.5 to 18.7 mW/cm^2 . In addition, propylene carbonate was used as cleaning agent keeping the different parts into a bath with agitation for 24 h and then air-dried at room temperature for 48 h.

2.5. Thermal treatments

The printed parts were subjected to different thermal cycles for debinding and sintering. At first, a thermogravimetric analysis and differential scanning calorimetry (TGA/DSC) were performed (TGA/SDTA 851e, Mettler Toledo, USA) after drying in order to design the thermal cycles for debinding process. The measurements were carried out from 50 °C to 700 °C with a heating rate of 5 °C/min in air.

Once the optimal temperatures and heating rates were determined for each step of the thermal cycles, specific thermal treatments were designed to debind the printed parts of the four studied formulations

without causing cracks or delamination (Fig. 1).

After debinding, the brown zircon parts were sintered at different temperatures (1450, 1500, 1550, 1600 °C) for 2 h using a conventional electric furnace (Nabertherm HTCT01/16, Germany) with heating/cooling rates of 5 °C/min. After sintering, the relative densities were determined by Archimedes' method (water immersion) using a value of 4.56 g/cm³ as theoretical density (TD) of zircon.

2.6. Characterisation of the printed bodies

At first, the absorbance spectra of printed parts obtained by using the different slurries and different printing parameters were measured by a Fourier transform infra-red spectrometer (FTIR Bruker Tensor 27, USA) to gain some information regarding the UV-light polymerization process. The samples were measured as prepared using the Pike Miracle single-bounce attenuated total reflectance (ATR) cell equipped with a ZnSe single crystal.

The crystalline phases of the starting zircon powder and final sintered parts were identified by X-ray diffraction (XRD; Advance diffractometer, Bruker Theta-Theta, Germany) using Cu K α radiation at a working power of 40 kV and 30 mA, a measurement range of 2 θ between 10° and 80°, a scanning speed of 1.5 s/step and a step size of 0.05°. For this purpose, the sintered parts were first ground with a tungsten carbide mortar and passed through a sieve with a mesh size of 63 μ m.

The microstructure of the different green and sintered pieces was observed by field emission gun scanning electron microscopy (FEG-SEM, Hitachi S4700 Type I, Japan). In the case of sintered bars, the specimens were polished down to 1 μ m using diamond paste and subsequently thermally etched at temperatures 15 % lower than the sintering temperature (°C). In addition, the porosity and average pore size of green printed parts were determined by image analysis (ImageJ software, National Institutes of Health, USA) from micrographs taken at 10,000x magnification.

3. Results and discussion

3.1. Particle size and rheological study of slurries

In order to obtain homogeneous and suitable UV-curable slurries of zircon powder, firstly the Solsperse 41,000 was selected as dispersing agent given its successful steric stabilization mechanism already previously reported for similar formulations [39–41]. To determine the required amount of dispersant with respect to the ceramic powder, a particle size study was performed on diluted slurries (6 vol% of solids) of this material, kept for 3 days on a rolling bench with zirconia balls and using benzyl alcohol as dispersion medium. It is worth mentioning that both benzyl alcohol and cyclohexanol are protic organic solvents (proton donors) mixed together with the aprotic monomers/oligomers in the final DLP formulations, which could improve the dispersion of zircon powder by varying the energy required for particles wettability and by adsorption of protons on the particles surface which provide some electrostatic character to the dispersion mechanism [42]. As can be observed in Fig. 2a, the particle size distribution curve of zircon without deflocculant addition is shifted towards larger particle sizes than indicated by the manufacturer due to the presence of agglomerates. After dispersant addition (0.5 and 1 wt%), however, narrower particle size distribution centred at 0.9 μ m could be achieved, in agreement with the technical specifications of the starting raw material. However, both dispersant concentrations appear to yield similar particle size distributions. On the other hand, Fig. 2b shows the flow curves obtained for concentrated slurries (40 vol% zircon) after planetary mill treatment from rotational rheometry. Clear viscosity differences can be observed between all dispersions, including those prepared with 0.5 and 1 wt% Solsperse 41,000. 1 wt% of dispersant addition provides a lower viscosity and a near Newtonian behaviour. Furthermore, none of the slurries reveal any thixotropic behaviour. Given those results, 1 wt% was fixed for the following as the optimum amount of deflocculant with respect to the zircon powder for preparation and optimisation of UV-curable ceramic resins.

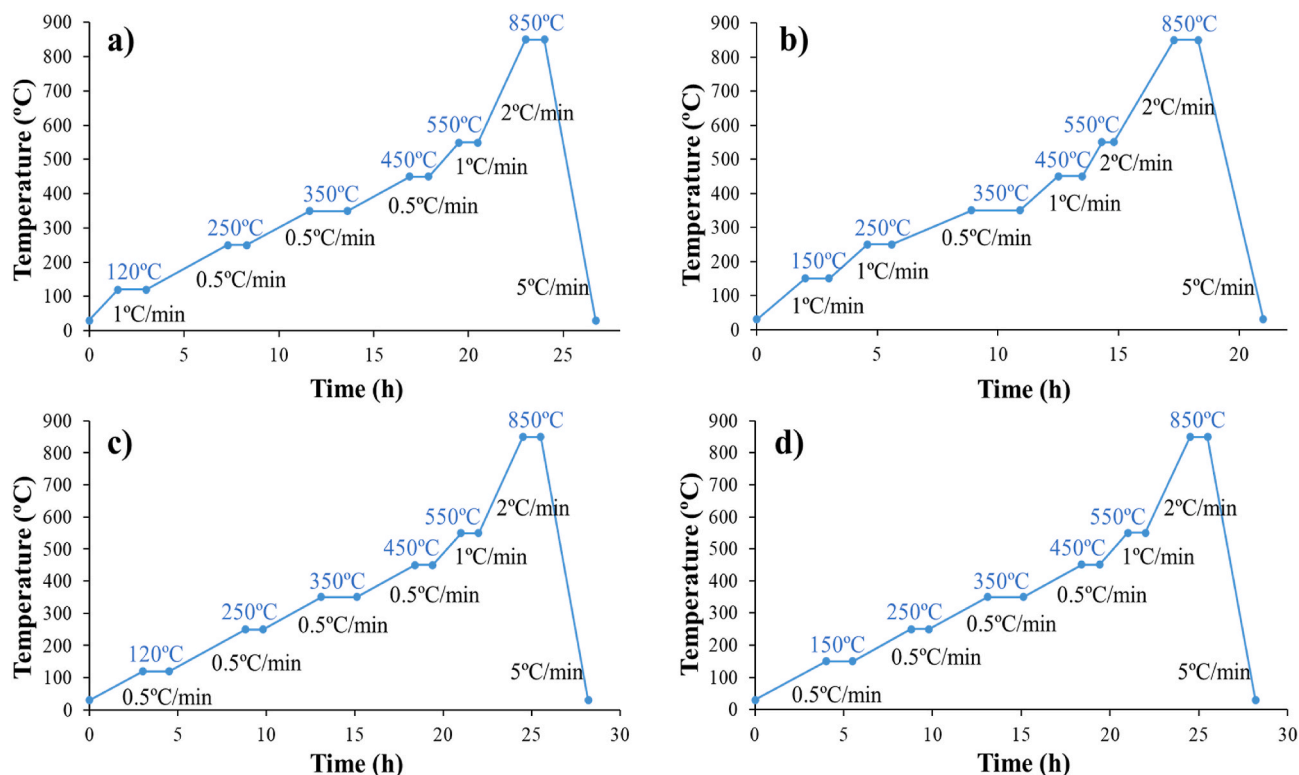


Fig. 1. Debinding thermal cycles for DLP parts printed using the a) BA25, b) CH25, c) BA35 and d) CH35 zircon slurries.

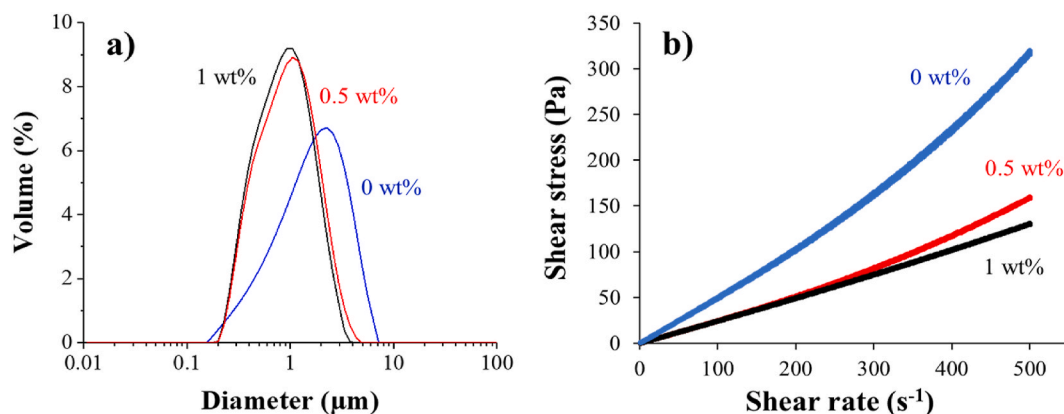


Fig. 2. Effect of dispersant concentration on a) particle size of zircon in diluted slurries (6 vol%) and b) flow curves of zircon concentrated slurries (40 vol%).

Once the optimum amount of dispersant was fixed (1 wt%), the particle size evolution was also studied using different homogenisation processes to optimise the slurries. Fig. 3 shows the particle size distribution curves of zircon powder in BA25 polymeric mixture after 1 h of propeller mixing, after 20 min of planetary ball milling and after 24 h of roll bench homogenisation only with 3 mm zirconia balls added to the container. As it can be observed, the fresh suspension homogenised solely by propeller mixing for 1 h still shows some agglomerates of around 100 μm, indicating that the deflocculant polymeric chains had insufficient time to be fully adsorbed on the particles surface and/or insufficient energy was provided to break the agglomerates. On the other hand, for the suspension left for 24 h homogenizing on the rolling bench with zirconia beads no more large agglomerates could be observed. The suspension shows a monomodal size distribution curve, with a distinct shoulder centred around 1 μm, indicative of a residual fraction of small agglomerates. Finally, the slurry treated for 20 min in the planetary mill shows a narrow monomodal particle size curve centred at 0.9 μm, confirming the necessity of higher energy contribution needed to break the agglomerates, in parallel homogenizing the suspension. Planetary ball milling was thus selected for the preparation of the different slurries.

Once the optimum dispersant content and the dispersion method were set, different slurries were prepared by dispersing the zircon powder into the four liquid organic mixtures (BA25, CH25, BA35 and CH35). As for the solids content, viscosity measurements of suspensions prepared in BA25 liquid phase were performed at 40, 45 and 48 vol%

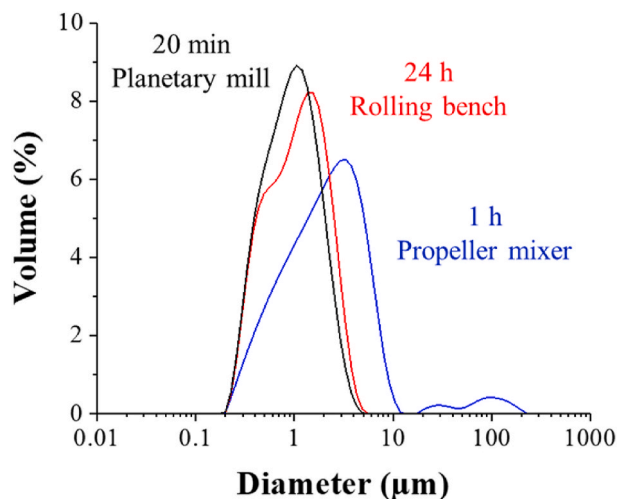


Fig. 3. Effect of mechanical treatments on the particle size distribution of zircon powder in concentrated BA25 slurries (40 vol%).

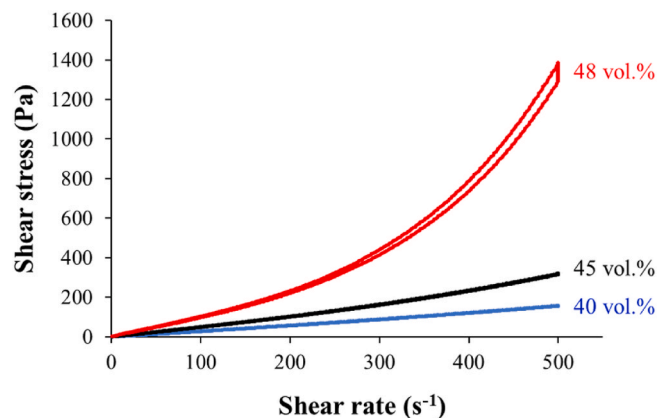


Fig. 4. Flow curves of BA25 slurries at zircon contents of 40, 45 and 48 vol%.

(Fig. 4 shows the corresponding flow curves). It was observed that the suspensions prepared with 40 and 45 vol% solids content showed a low viscosity (0.31 against 0.62 Pa s at 500 s⁻¹, respectively), suitable for DLP printing. On the other hand, suspensions prepared at 48 vol% solids had a higher viscosity (2.7 Pa s at 500 s⁻¹) and exhibited a strong shear thickening effect from 100 s⁻¹ onwards with a remarkable thixotropic cycle, undesirable for DLP 3D printing. Thus, a solid content of 45 vol% was fixed for the preparation of different UV-curable ceramic slurries, maintaining a suitable rheological behaviour for DLP 3D printing and a solid content high enough to avoid a large shrinkage during the debinding process that may favour the appearance of microcracks or delamination in the brown parts [33–38].

Once the different slurries were prepared with an optimised solids loading of 45 vol%, rheological measurements were performed for the four formulations to compare the different homogenisation procedures, i.e., propeller mixing for 1 h, propeller plus 20 min of planetary ball milling and then, after keeping them for 24 h on the rolling bench with zirconia balls. Fig. 5 shows the viscosity curves of the four different slurries after each step of their mechanical treatment. As can be observed, all of them show a higher viscosity and specially a clear shear thickening effect after only 1 h of propeller mixing, which indicates that the powder is not properly dispersed into the liquid phase. After planetary mill treatment, it can be observed that the viscosity of all the slurries decreased with additionally the disappearance of the shear thickening effect at higher shear rates. Despite of the effectiveness of the planetary milling process, it can also be observed how the rheological behaviour can be further optimised by keeping the slurries for 24 h more on the rolling bench together with 3 mm zirconia balls, leaving time for surface speciation reactions with the dispersant and slurry homogenisation [43,44]. Moreover, there is a difference in the rheological

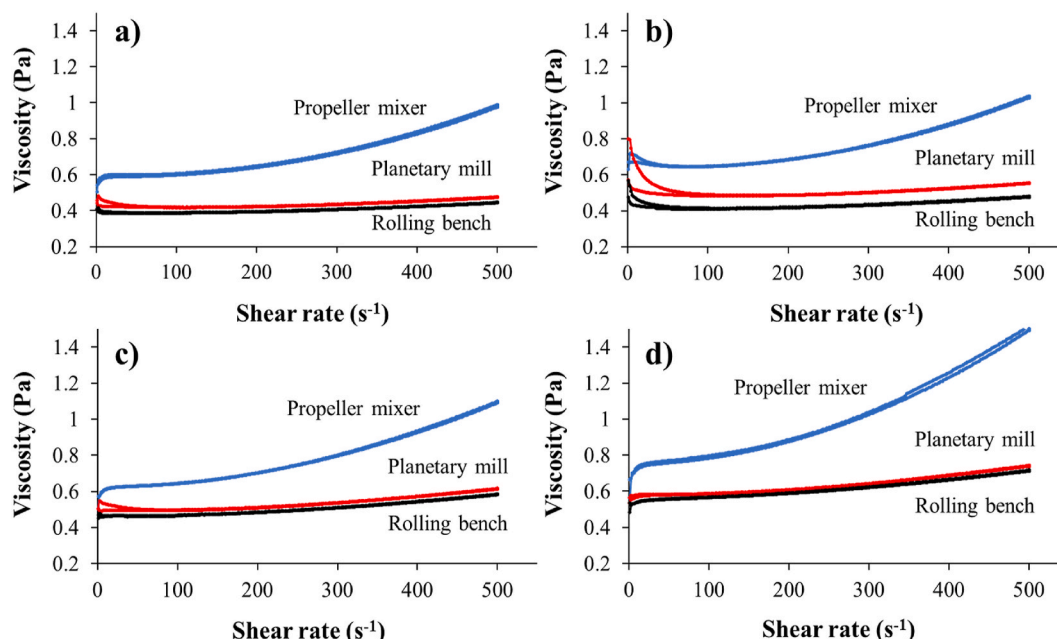


Fig. 5. Viscosity curves of a) BA25, b) BA35, c) CH25, d) CH35 slurries at 45 vol% zircon content after 1 h of propeller mixing, after 20 min more of planetary ball milling and after 24 h more in rolling bench with 3 mm zirconia balls.

behaviour between the slurries prepared dispersing the zircon powder into the organic mixtures containing benzyl alcohol or cyclohexanol as the solvent. In the case of the BA slurries, and especially for those with higher concentration of solvent in the liquid phase (BA35), a shear thinning effect can be observed at very low shear rates, which is desired for this type of DLP formulations since it avoids the settling of ceramic material between layers during the printing process [45,46]. On the other hand, the CH35 slurry shows rather Newtonian behaviour (same viscosity value at very low shear rates), which could lead to a slight sedimentation of zircon powder between one layer and the next one. Even so, all different suspensions present a suitable viscosity value (around 0.5 Pa s at 100 s^{-1}) for the DLP printing technique, since this type of light-curing resins must exhibit viscosities of less than 3 Pa s above 100 s^{-1} for proper flowability and homogenisation by the scraper on the printer vat [35,36,38].

3.2. DLP printing process

After optimisation of all UV-curable zircon slurries, different parts were printed by DLP obtaining solid bars and scaffolds with different sizes. The standard dimensions (SD) for printed bars were $24 \times 6 \times 4 \text{ mm}$ and for scaffolds $10 \times 10 \times 10 \text{ mm}$, but other samples were prepared by applying scaling factors (SF) of 0.7 and 0.5 in the case of bars ($16.8 \times 4.2 \times 2.8$ and $12 \times 3 \times 2 \text{ mm}$, respectively) and 0.7 in the case of scaffolds ($7 \times 7 \times 7 \text{ mm}$). At first, a printing parametric study was performed for each ceramic/polymeric system resulting in different optimum printing parameters for each one (Table 1). In the case of BA systems, the required energy dose was higher than for CH systems ($15\text{--}21$ vs. $10\text{--}15 \text{ mJ/cm}^2$), whilst in general the energy dose increased with higher nonreactive solvent concentration (e.g. BA and CH) such as 15 mJ/cm^2

Table 1
Optimum DLP printing parameters for each UV-curable zircon slurry.

Printing parameters	BA25	BA35	CH25	CH35
Layer thickness (μm)	25	25	25	25
Exposure time (s)	2.5	3	2.5	3
Exposure intensity (mW/cm^2)	6	7	4	4
Energy dose (mJ/cm^2)	15	21	10	12

for the BA25 against 21 mJ/cm^2 for the BA35 slurry. Moreover, after fixing the required energy dose, the exposure time and intensity were also varied from 1 to 4 s and from 18.7 to 2.5 mW/cm^2 , respectively, in order to investigate the effect of the energy ramp. Parts printed with longer exposure times and lower intensities showed a greater resolution and homogeneity, with a critical ratio between both parameters to achieve proper adhesion between layers (maximum of 3 s and minimum of 4 mW/cm^2). After printing, the different parts were cleaned in propylene carbonate for 24 h with agitation, removing the non-polymerized slurry. Then, the pieces were air-dried at room temperature for 48 h.

Fig. 6 shows the optical microscope images for the different parts obtained by DLP. As can be observed in the case of bars, those obtained from BA slurries (a) were homogeneous without any visible traces of cracks and delamination. In contrast, a delamination problem could be observed in parts produced from CH containing slurries after drying (b and c). This problem could however be reduced by reducing the part thickness (d). It is believed that this delamination issue for bars obtained

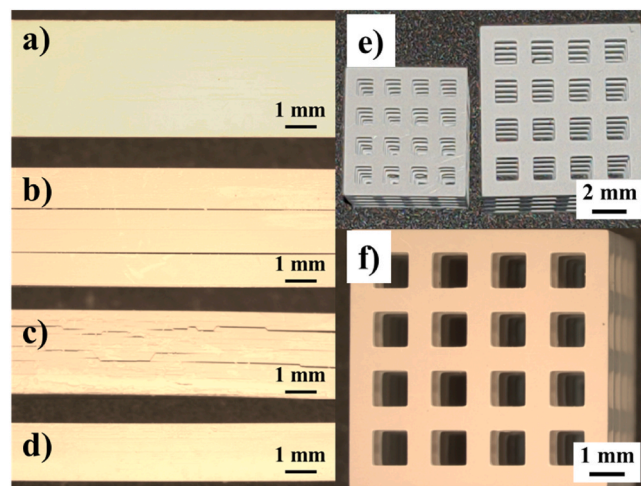


Fig. 6. Optical microscope images of solid bars of a) BA25 (SD), b) CH25 (SD), c) CH25 (SF 0.7), and d) CH25 (SF 0.5) and scaffolds of e) CH25 (SD and SF 0.7), and f) CH35 (SF 0.7).

from CH slurries is related to the pore structure and capillary pressures and could be solved by a supercritical CO₂ drying process [47]. This would, however, complexify the process and render it more expensive compared to BA bars that can be easily dried at room conditions. On the other hand, it was not possible to obtain scaffolds by printing BA slurries, since the strength of the struts was insufficient to maintain the structure under the tensile forces exerted by the printer during the tilting step used for the separation of successive layers (even at the slowest tilting speed). This breakage of the scaffolds could not be solved by increasing the exposure energy dose, as overcuring caused the parts to remain attached to the vat instead of to the printing platform. However, in the case of the scaffolds printed with CH25 (e) and CH35 (f) slurries, the struts had sufficient tensile strength to be printed without any delamination effect since the width of the struts is 1 mm in the case of the largest pieces (less than the thickness of the smallest bars).

The green printed parts were characterised by FT-IR following the photopolymerization printing process. Fig. 7 shows the absorbance spectra of pieces printed with BA and CH slurries and using the optimum energy dose for each one. None of them exhibited the characteristic peak at 1500–1600 cm⁻¹ typical of the C=C double bonds, indicating that all monomers fully reacted and therefore no vinyl groups from the starting acrylates are present in the final printed parts. It can also be observed in all cases a characteristic signal of C–H bonds around 2900 cm⁻¹ corresponding to polymeric chains that have been formed during the photopolymerization process. On the other hand, comparing the spectra of BA25/CH25 with BA35/CH35 pieces, a clear difference can be observed from the appearing of a double peak around 1750 cm⁻¹ in the case of the parts printed with higher solvent content slurries. This double peak corresponds to carbonyl groups and may be due to propylene carbonate (e.g. cleaning agent) with different C=O bonds compared to the acrylate-type polymeric chains being retained in the internal structure of the parts. The reasons for this have not been investigated in detail, but may be due to a changed pore structure, where larger cavities connected with smaller pore channel may trap the propylene carbonate due to capillary pressure effects. Furthermore, comparing the relative intensities between the two types of carbonyl groups, it is noticeable that the retention of propylene carbonate was higher in the case of BA35 parts, which suggest a higher porosity grade and a less homogeneous pore size distribution with the presence of very fine channels. This could favour the debinding process avoiding the appearance of microcracks or delamination during volatilisation of organic compounds while making it possible to obtain fully densified materials after sintering.

The microstructure of the green printed parts was also studied to

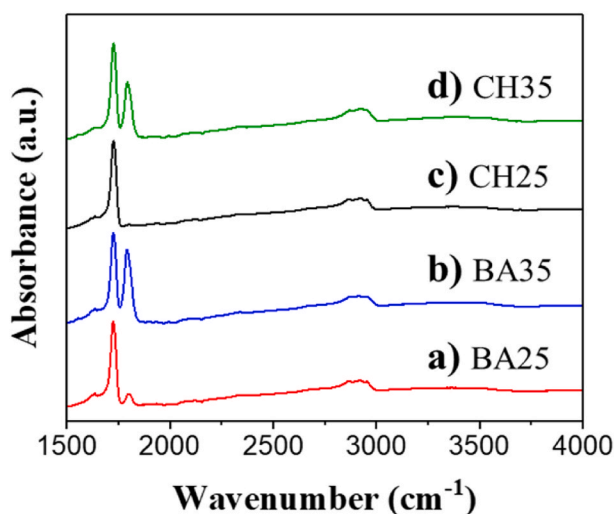


Fig. 7. FTIR absorbance spectra of a) BA25, b) BA35, c) CH25, d) CH35 printed parts after cleaning and drying for 24 h.

corroborate the hypothesis drawn from the FTIR results regarding the infiltration of cleaning agent into the internal porosity. Fig. 8 shows the cross-section micrographs taken at 10,000x magnification on pieces produced from the four different slurries. As can be observed, the porosity is higher at higher non-reactive solvent concentrations into the organic phases (13.6 % and 11.4 % for b and d with respect to 12.2 % and 10.6 % for a and c, respectively). Moreover, analysing the micrographs obtained for BA35 and CH35 parts (b and d respectively) using Image J software, the resulting porosity value was higher for BA35 (13.6 % against 11.4 %) and its average pore size was smaller (0.21 against 0.31 μ m). Also, it is noticeable that the porosity is more homogeneously distributed in the case of parts printed with BA slurries, which could favour the debinding process while ensuring a high densification of the material after sintering. The less homogeneous distribution of cyclohexanol as a solvent could be due to a polymerization-induced phase separation process, resulting in a polymer-rich phase that forms the matrix together with the ceramic particles and a polymer-poor phase providing this type of larger cavity porosity [47,48].

3.3. Debinding and sintering

In order to properly design the thermal programs for the debinding process, thermogravimetry and differential scanning calorimetry of the different as-printed parts were performed. Fig. 9 shows the TG/DSC graphs of pieces printed with the four different slurries. Three main weight losses can be observed in all the samples, the first one corresponding to the solvent evaporation and the other two at higher temperature to the combustion of the polymeric chains. It is notorious that the loss of mass corresponding to solvent evaporation is produced at lower temperatures (100–180 °C) in the case of BA parts (a and b). In contrast, solvent volatilisation in CH ones occurs over a wider temperature range (100–300 °C), which seems to be related to the less homogeneous distribution of cyclohexanol as solvent in the internal structure of the pieces (as observed in the different porosity distribution in Fig. 8). This is followed in all cases by the combustion of the polymers with two main mass losses at 350 and 450 °C. In addition, three exothermic peaks are observed in the DSC curves at approximately 260, 380 and 460 °C, the last two being considerably more intense. These correspond to the volatilisation of the polymer chains in three partial combustions or decompositions. Based on these results, the thermal cycles shown in Fig. 1 were designed to perform the debinding process of all parts with no cracking or delamination.

Once the different pieces were successfully debinded, the brown zircon parts were sintered at different temperatures (1450, 1500, 1550, 1600 °C) for 2 h in a conventional air furnace. The density of the pieces increases with sintering temperature, as expected due to the low densification of zircon as a refractory ceramic material, being the highest for those sintered at 1600 °C (values shown in Table 2). In addition, the density of the parts was slightly higher for those printed using slurries with a higher proportion of solvent (96.8 % for BA25 vs. 97.5 % for BA35 and 96.2 % for CH25 vs. 96.7 % for CH35), which could be related to the generation of microdefects during debinding and may have potentially been equalized by extending the dwell time for the former. It is also worth noting that the density of BA parts was slightly higher than that of CH ones and also that the standard deviation in density measurements for different parts of the same type was considerably higher in the case of CH ones (Table 2). This reinforces the hypothesis about the poor distribution of cyclohexanol as the solvent in the internal structure of the as-printed parts and therefore the non-uniformly distributed porosity that it creates in these pieces, hindering the subsequent volatilisation of polymers during the debinding process and densification by sintering. As previously mentioned, this CH distribution into the parts structure could be related to a photopolymerization-induced phase separation process which may be minimised by increasing the energy dose rate during printing, reducing the exposure time and increasing the intensity to prevent solvent

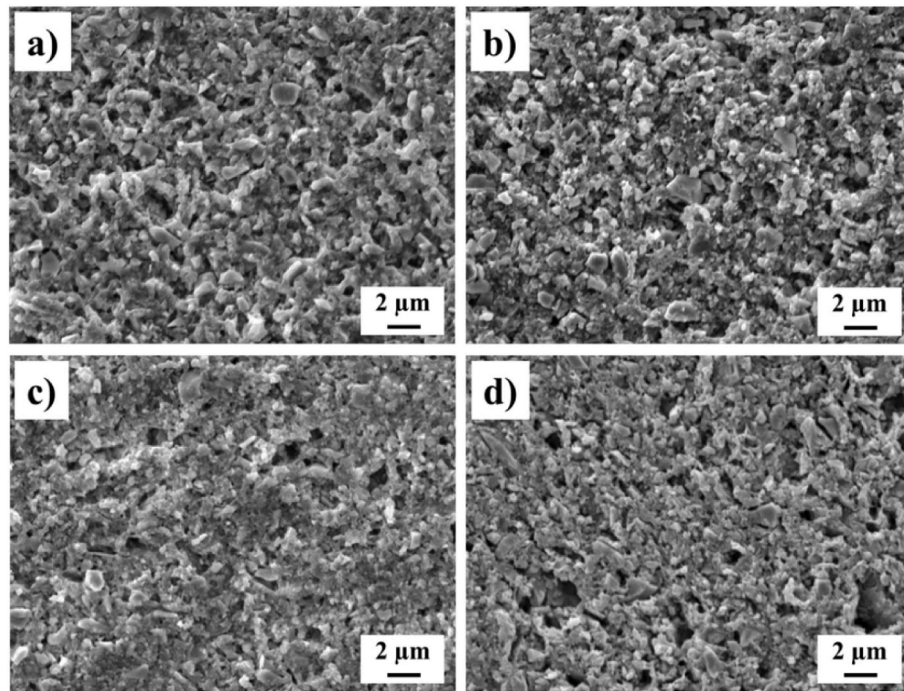


Fig. 8. SEM micrographs of a) BA25, b) BA35, c) CH25, d) CH35 cleaned and dry printed parts. Magnification 10,000x.

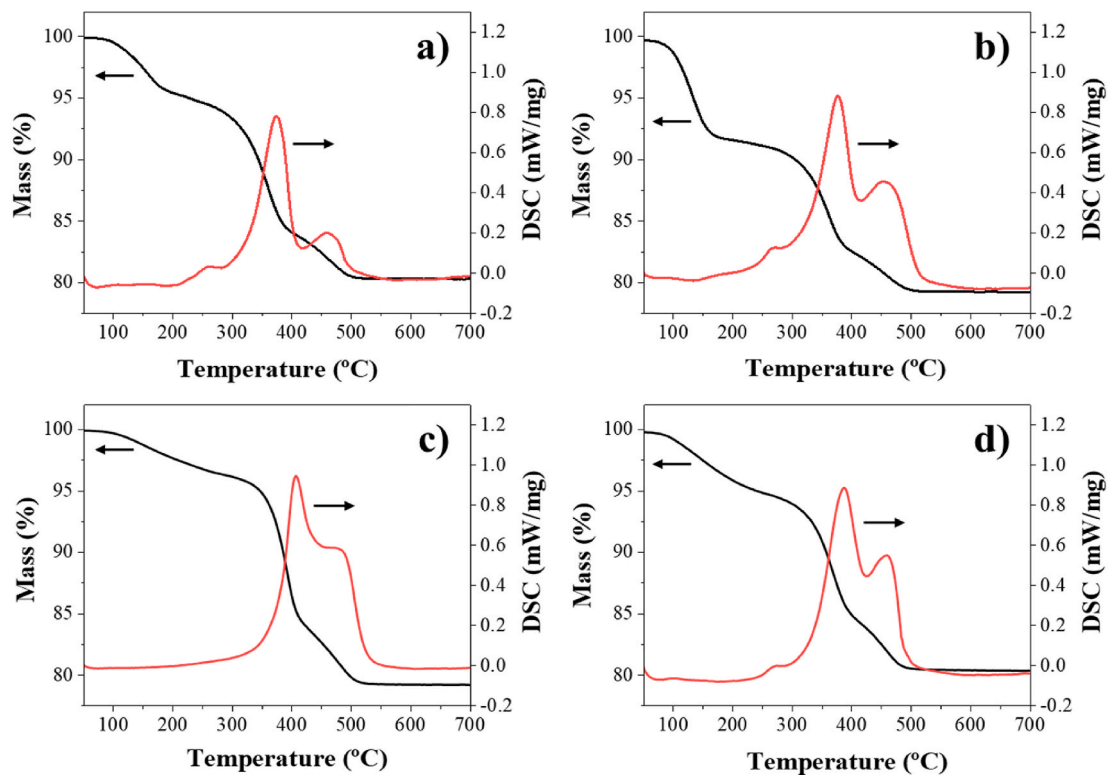


Fig. 9. TG/DSC curves of a) BA25, b) BA35, c) CH25, d) CH35 as-printed parts.

migration to polymer-poor areas [47].

3.4. XRD characterisation

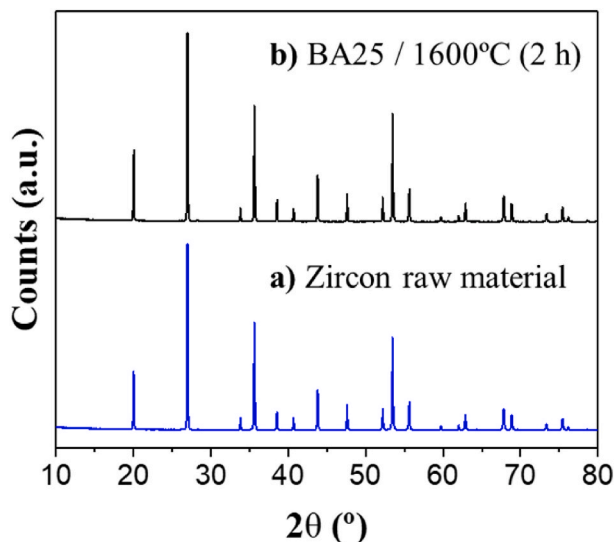
The sintered bodies were characterised by XRD to determine whether the zircon material underwent decomposition into SiO_2 and ZrO_2 by the different mechanical treatments applied in the optimisation of the UV-

curable suspensions and during the high temperature sintering process. Fig. 10 shows the diffractograms of the starting zircon powder as received and of a part printed using the BA25 slurry (45 vol% zircon) and sintered at 1600 °C for 2 h. As can be observed by comparing both patterns, the zircon material sintered at high temperature (close to its decomposition temperature of 1675 °C [3]) shows exactly the same peaks as the raw material powder, without traces of zirconia or quartz.

Table 2

Density of DLP-printed bars sintered at 1600 °C for 2 h.

Sintered bars	Density (g/cm ³)	Density (%TD)
BA25	4.404 ± 0.009	96.8 ± 0.2
BA35	4.436 ± 0.013	97.5 ± 0.3
CH25	4.377 ± 0.044	96.2 ± 1.0
CH35	4.400 ± 0.057	96.7 ± 1.3

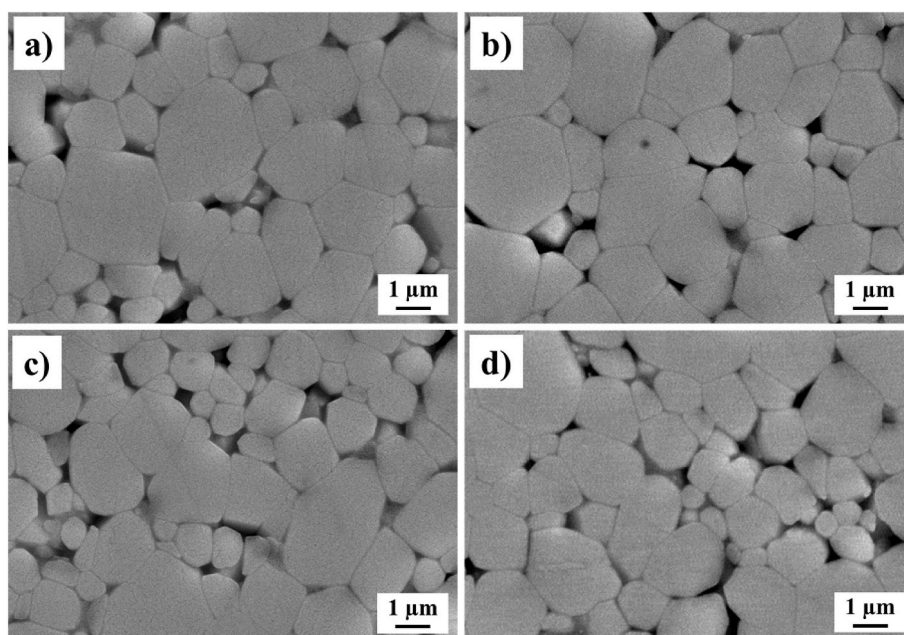
**Fig. 10.** Diffractograms of a) zircon raw material and b) BA25 printed part sintered at 1600 °C for 2 h.

This demonstrates the suitability of the processing of the starting ceramic powder and the subsequent treatments, including shaping and sintering, to obtain dense materials with a high crystalline purity (without the presence of glassy silica phase) which will improve the thermo-mechanical properties of the final pieces.

3.5. Microstructural characterisation of sintered parts

The microstructure of zircon parts sintered at different temperatures (1450, 1500, 1550, 1600 °C) for 2 h was observed by FEG-SEM. Fig. 11 shows the micrographs obtained from the bars with highest densities (1600 °C/2h). The SEM observations and the relative densities demonstrate that the microstructure and densification grade were similar to zircon bodies obtained by other forming techniques such as slip casting [21–23], gelcasting [24] or uniaxial/isostatic pressing of activated pure powders [10–12,15,16], prior to pressureless sintering at the same temperature for similar or longer dwell times. As previously commented, values up to 97.5 % of the theoretical density were achieved for BA35 parts, which supposes a rather high densification degree taking into account the limited sinterability of zircon as compared with values reported by other authors who conventionally sintered zircon specimens ($\leq 96\%$ TD). Moreover, since no great difference was observed in the reported density values for the different bars (Table 2), the microstructure of these was also quite similar, with the materials obtained using slurries with higher concentrations of non-reactive solvents in the organic phase formulation appearing to be slightly denser (b and d compared to a and c). In addition to the drying delamination problems for CH bars previously discussed, a slightly higher density of BA parts compared to CH ones could also be observed. This suggests again a more homogeneous distribution of benzyl alcohol as the solvent in the internal structure of the printed parts and therefore, the more suitable porosity arrangement that favours the debinding process and the sinterability of brown bodies.

Finally, Fig. 12 shows the micrographs taken on scaffolds obtained using the CH slurries and sintered at 1600 °C for 2 h. As can be observed, no delamination or cracking occurred in the parts and the high resolution achieved by the DLP printer results in a perfect finish on the square morphology of the piece's channels and struts (Fig. 12a). Thus, the final width of the sintered scaffold struts is around 565 μm (620 μm for the green part, which represents a 9 % shrinkage). In contrast, the square channels show an 850 μm side window (1000 μm for the green part), which means a dimensional reduction of 15 % after debinding and sintering. In addition, Fig. 12b shows the corner of one of the square channels at higher magnification, making it possible to better observe the high resolution of the DLP 3D printing technique and the slightly rounded finish that characterises this technique for obtaining sharp

**Fig. 11.** SEM micrographs of polished a) BA25, b) BA35, c) CH25, d) CH35 bars sintered at 1600 °C for 2 h. Magnification 10,000x.

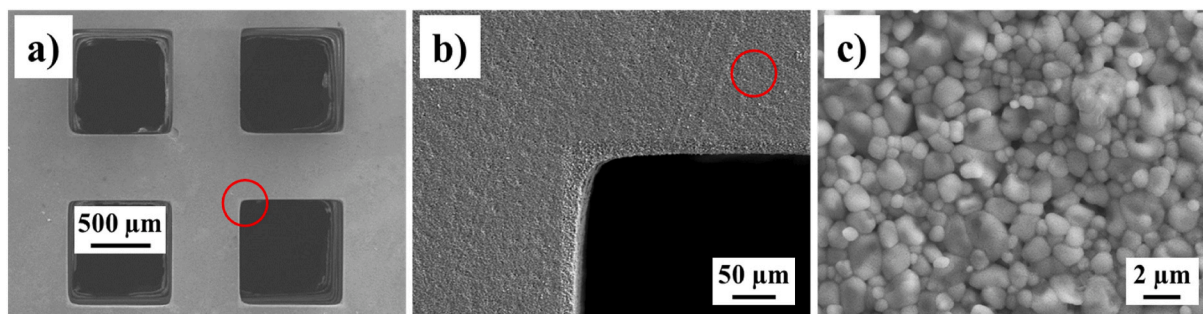


Fig. 12. SEM micrographs of CH25 scaffold sintered at 1600 °C for 2 h. Magnification a) 35x, b) 250x, c) 5000x.

morphologies. Lastly, Fig. 12c shows the microstructure of one of the struts at higher magnification, demonstrating the adequacy of the debinding process and the high densification obtained by conventional sintering.

4. Conclusions

Different UV-curable liquid phases were developed by mixing monomer/oligomer compounds with benzyl alcohol and cyclohexanol as non-reactive solvents and porogenic agents. Ceramic resins were obtained introducing a zircon powder (45 vol%) into the organic phases by means of a steric-mechanism dispersion. The rheological behaviour of the slurries was optimised by ball planetary milling (300 rpm/20 min) and maintaining them in rolling bench for 24 h. Different bars and scaffolds were printed by DLP using the different ceramic slurries and optimising the printing parameters (energy doses of 15–21 mJ/cm² for BA parts and 10–15 mJ/cm² for CH ones). The resulting porosity grade and distribution was different for parts printed using BA and CH as solvents (13.6 % for BA35 and 11.4 % for CH). The higher porosity grade and more homogeneous distribution in BA green parts led to solvent volatilisation occurring at lower temperatures during the debinding process (100–180 °C for BA vs. 100–300 °C for CH). Successful thermal debinding programs were designed for each type of formulation obtaining crack-free zircon brown pieces. The different brown parts were pressureless sintered (1600 °C/2h) obtaining slightly higher densities for BA ones (97.5%TD for BA35 vs. 96.7%TD for CH35) and for those produced with higher solvent concentration into the UV-curable liquid phase (96.8%TD for BA25 and 97.5%TD for BA35). It is worth noting that these density values are rather high compared to zircon materials obtained by other processing techniques and pressureless sintered ($\leq 96\%$ TD) including isostatic pressing and colloidal forming.

Declaration of competing interest

The authors declare that they have no known competing financial interests or personal relationships that could have appeared to influence the work reported in this paper.

Acknowledgements

This research was funded by the Spanish Ministry of Science and Innovation, the State Research Agency (AEI) and the European Regional Development Fund (FEDER) under project PID2021-124521OB-I00, the JECS Trust mobility grant with contract number 2023345 and pre-doctoral fellowship PRE2019-091092.

References

- [1] H. Aral, G.J. Sparrow, K. McDonald, T.E. Norgate, Pure zircon process for removing radionuclides from zircon concentrates, *Miner. Process. Extr. Metall. (IMM Trans. Sect. C)* 116 (2007) 145–151.
- [2] N.M. Rendtorff, L.B. Garrido, E.F. Aglietti, Effect of the addition of mullite–zirconia to the thermal shock behavior of zircon materials, *Mater. Sci. Eng.* 498 (2008) 208–215.
- [3] A. Kaiser, M. Lobert, R. Telle, Thermal stability of zircon (ZrSiO₄), *J. Eur. Ceram. Soc.* 28 (2008) 2199–2211.
- [4] R. Terki, G. Bertrand, H. Aourag, Full potential investigations of structural and electronic properties of ZrSiO₄, *Microelectron. Eng.* 81 (2005) 514–523.
- [5] N.M. Rendtorff, L.B. Garrido, E.F. Aglietti, Thermal shock resistance and fatigue of zircon–mullite composite materials, *Ceram. Int.* 37 (2011) 1427–1434.
- [6] I.G. Mel'nikova, T.A. Nesterova, I.V. Razdol'skaya, Zircon refractories for glass-melting, *Glass Ceram.* 42 (1985) 295–298 (review).
- [7] R.S. Pavlik, H.J. Holland, E.A. Payzant, Thermal decomposition of zircon refractories, *J. Am. Ceram. Soc.* 84 (12) (2001) 2930–2936.
- [8] E. Cañas, E. Rosado, C. Alcázar, M.J. Orts, R. Moreno, E. Sánchez, Challenging zircon coatings by suspension plasma spraying, *J. Eur. Ceram. Soc.* 42 (2022) 4369–4376.
- [9] E. Rosado, E. Cañas, P. Recio, E. Sánchez, R. Moreno, ZrSiO₄/ZrO₂ thermal barrier coatings produced by suspension plasma spraying, *J. Eur. Ceram. Soc.* 44 (1) (2023) 460–470.
- [10] K.B. Lee, J.B. Kang, Sintering behavior of zircon with SiO₂, *Korean J. Mater. Res.* 18 (2008) 604–609.
- [11] M.C. Anjali, P. Biswas, D. Chakravarty, U.S. Hareesh, Y.S. Rao, R. Johnson, Low temperature in-situ reaction sintering of zircon-alumina composites through spark plasma sintering, *Sci. Sinter.* 44 (2012) 323–330.
- [12] M.R. Gauna, J.M. Martínez, M.S. Conconi, G. Suárez, N.M. Rendtorff, Effect of TiO₂ in fine zircon sintering and properties, *Sci. Sinter.* 53 (2021) 267–283.
- [13] R. Moreno, J.S. Moya, J. Requena, Slip casting of zircon, *J. Mater. Sci. Lett.* 5 (1986) 127–128.
- [14] N.M. Rendtorff, S. Grasso, C. Hu, G. Suarez, E.F. Aglietti, Y. Sakka, Dense zircon (ZrSiO₄) ceramics by high energy ball milling and spark plasma sintering, *Ceram. Int.* 38 (2012) 1793–1799.
- [15] X. Carbonneau, M. Hamidouche, C. Olagnon, G. Fantozzi, R. Torrecillas, High temperature behaviour of a Zircon ceramic, *Key Eng. Mater.* 132–136 (1997) 571–574.
- [16] M. Gauna, M. Conconi, G. Suarez, E. Aglietti, N. Rendtorff, Dense zircon (ZrSiO₄) ceramics by a simple milling-sintering route, *Sci. Sinter.* 50 (2018) 15–28.
- [17] Y. Ding, Z. Jiang, Y. Li, Y. Tang, J. Li, X. Dong, H. Dan, Y. Yang, T. Duan, Low temperature and rapid preparation of zirconia/zircon (ZrO₂/ZrSiO₄) composite ceramics by a hydrothermal-assisted sol-gel process, *J. Alloys Compd.* 735 (2018) 2190–2196.
- [18] P. Tartaj, Zircon formation from nanosized powders obtained by a reverse micelle process, *J. Am. Ceram. Soc.* 88 (1) (2005) 222–224.
- [19] P. Tartaj, L.C. De Jonghe, Preparation of nanospherical amorphous zircon powders by a microemulsion-mediated process, *J. Mater. Chem.* 10 (12) (2000) 2786–2790.
- [20] P. Tartaj, J. Sanz, C.J. Serna, M. Ocaña, Zircon formation from amorphous spherical ZrSiO₄ particles obtained by hydrolysis of aerosols, *J. Mater. Sci.* 29 (24) (1994) 6533–6538.
- [21] R. Moreno, J.S. Moya, J. Requena, Slip casting of zircon, *J. Mater. Sci. Lett.* 5 (1986) 127–128.
- [22] R. Moreno, J.S. Moya, J. Requena, Slip casting of zircon by using an organic surfactant, *Ceram. Int.* 17 (1991) 37–40.
- [23] G. Suárez, S. Acevedo, N.M. Rendtorff, L.B. Garrido, E.F. Aglietti, Colloidal processing, sintering and mechanical properties of zircon (ZrSiO₄), *Ceram. Int.* 41 (2015) 1015–1021.
- [24] E. Rosado, C. Alcázar, P. Recio, R. Moreno, Near-net shaping of zircon compacts through agar gelation, *Eur. J. Mater.* 2 (2022) 407–421.
- [25] R. Moreno, Better ceramics through colloid chemistry, *J. Eur. Ceram. Soc.* 40 (3) (2020) 559–587.
- [26] N.M. Rendtorff, S. Grasso, C. Hu, G. Suárez, E.F. Aglietti, Y. Sakka, Zircon–zirconia (ZrSiO₄–ZrO₂) dense ceramic composites by spark plasma sintering, *J. Eur. Ceram. Soc.* 32 (2012) 787–793.
- [27] Y. Shi, X. Huang, D. Yan, Fabrication of hot-pressed zircon ceramics: mechanical properties and microstructure, *Ceram. Int.* 23 (1997) 457–462.
- [28] S. Huang, Q. Li, Z. Wang, X. Cheng, H. Wen, Effect of sintering aids on the microstructure and oxidation behavior of hot-pressed zirconium silicate ceramic, *Ceram. Int.* 43 (2017) 875–879.

- [29] B. Ozkan, F. Sameni, S. Karmel, D.S. Engström, E. Sabet, Binder stabilization and rheology optimization for vat-photopolymerization 3D printing of silica-based ceramic mixtures, *J. Eur. Ceram. Soc.* 43 (4) (2023) 1649–1662.
- [30] I.L. de Camargo, R. Erbereli, J.F.P. Lovo, R. Fortulan, C.A. Fortulan, Digital light processing additive manufacturing of in situ mullite-zirconia composites, *J. Eur. Ceram. Soc.* 42 (2022) 6025–6032.
- [31] Q. Lian, F. Yang, H. Xin, D. Li, Oxygen-controlled bottom-up mask-projection stereolithography for ceramic 3D printing, *Ceram. Int.* 43 (2017) 14956–14961.
- [32] O. Santoliquido, P. Colombo, A. Ortona, Additive manufacturing of ceramic components by digital light processing: a comparison between the “bottom-up” and the “top-down” approaches, *J. Eur. Ceram. Soc.* 39 (2019) 2140–2148.
- [33] D.A. Komissarenko, P.S. Sokolov, A.D. Evstigneeva, I.A. Shmeleva, A.E. Dosovitsky, Rheological and curing behavior of acrylate-based suspensions for the DLP 3D printing of complex zirconia parts, *Materials* 11 (12) (2018) 2350.
- [34] E. Johansson, O. Lidström, J. Johansson, O. Lyckfeldt, E. Adolfsson, Influence of resin composition on the defect formation in alumina manufactured by stereolithography, *Materials* 10 (2) (2017) 138.
- [35] I.L. Camargo, M.M. Morais, C.A. Fortulan, M.C. Branciforti, A review on the rheological behavior and formulations of ceramic suspensions for vat photopolymerization, *Ceram. Int.* 47 (9) (2021) 11906–11921.
- [36] M.L. Griffith, J.W. Halloran, Freeform fabrication of ceramics via stereolithography, *J. Am. Ceram. Soc.* 79 (10) (1996) 2601–2608.
- [37] B. Maciej Wozniakun, C. Yoram de Hazanun, C. Thomas Graule, Highly loaded UV curable nanosilica dispersions for rapid prototyping applications, *J. Eur. Ceram. Soc.* 29 (11) (2009) 2221–2229.
- [38] Z. Chen, Z. Li, J. Li, C. Liu, C. Lao, Y. Fu, C. Liu, Y. Li, P. Wang, Y. He, 3D printing of ceramics: a review, *J. Am. Ceram. Soc.* 39 (4) (2019) 661–687.
- [39] M. Borlaf, N. Szubra, A. Serra-Capdevila, W.W. Kubiak, T. Graule, Fabrication of ZrO₂ and ATZ materials via UV-LCM-DLP additive manufacturing technology, *J. Eur. Ceram. Soc.* 40 (4) (2020) 1574–1581.
- [40] M. Borlaf, A. Serra-Capdevila, C. Colominas, T. Graule, Development of UV-curable ZrO₂ slurries for additive manufacturing (LCM-DLP) technology, *J. Eur. Ceram. Soc.* 39 (13) (2019) 3797–3803.
- [41] P. Zubrzycka, M. Radecka, T. Graule, M. Stuer, Debinding of additively manufactured parts from spinel powders with particle sizes below 200 nm, *Ceram. Int.* 49 (2023) 11355–11367.
- [42] P. Zubrzycka, M. Radecka, T. Graule, M. Stuer, Metal cation complexes as dispersing agents for non-aqueous powder suspensions, *Ceram. Int.* 47 (2021) 18443–18454.
- [43] M. Stuer, P. Bowen, Colloidal processing and yield stress modeling towards dry pressed green bodies for transparent polycrystalline alumina, *Adv. Eng. Mater.* 16 (6) (2014) 774–784.
- [44] G. Montavon, T. Rabung, H. Geckeis, B. Grambow, Interaction of Eu(III)/Cm(III) with alumina-bound poly(acrylic acid): sorption, desorption, and spectroscopic studies, *Environ. Sci. Technol.* 38 (2004) 4312–4318.
- [45] N. Travitzky, A. Bonet, B. Dermeik, T. Fey, I. Filbert-Demut, L. Schlier, T. Schloridt, P. Greil, Additive manufacturing of ceramic-based materials, *Adv. Eng. Mater.* 16 (2014) 729–754.
- [46] A. Zocca, P. Colombo, C.M. Gomes, J. Günster, Additive manufacturing of ceramics: issues, potentialities, and opportunities, *J. Am. Ceram. Soc.* 98 (2015) 1983–2001.
- [47] Z. Dong, H. Cui, H. Zhang, F. Wang, X. Zhan, F. Mayer, B. Nestler, M. Wegener, P. A. Levkin, 3D printing of inherently nanoporous polymers via polymerization-induced phase separation, *Nat. Commun.* 12 (2021) 247.
- [48] M. Seo, M.A. Hillmyer, Reticulated nanoporous polymers by controlled polymerization-induced microphase separation, *Science* 336 (2012) 1422–1425.